RSC Advances

PAPER

View Article Online
View Journal | View Issue

Cite this: *RSC Adv.*, 2025, **15**, 5808

Improving the efficiency of Cr(VI) reduction and adsorption by Fe_3O_4 using ZSM-5 zeolite support prepared through various methods†

Nichapha Senamart,[a] Worapol Yingyuen,[a] Waranya Obrom,[a] Tatchapol Nanmong,[a] Surangkhana Budsombat,[a] Jatuporn Wittayakun,[b] Sanchai Prayoonpokarach[b] and Sirinuch Loiha *[a]

The study involved the synthesis of magnetite (Fe_3O_4) and zeolite-supported Fe_3O_4 (Fe/Z) using co-precipitation (COP) and hydrothermal (HYD) methods which proved effective for removing Cr(VI) from contaminated water. X-ray diffraction (XRD) analysis showed that the Fe_3O_4 phase had a cubic crystal structure. The COP method resulted in lower crystallinity compared to the HYD method. The different preparation methods also led to variations in the morphologies and sizes of the Fe_3O_4 particles. The HYD-prepared sample exhibited a uniform spherical shape with sizes of 400–500 nm, while the COP-prepared samples showed rod-like and granule shapes with smaller particle sizes of 20–50 nm. The study also investigated the adsorption ability and reducibility of Cr(VI) on the Fe_3O_4 adsorbents. It was found that the crystallinity, shapes, and sizes of Fe_3O_4 significantly influenced the adsorption capacity and stability of the Cr-adsorbed species. Additionally, this work demonstrated that the zeolite supports enhanced the adsorption capabilities of Fe_3O_4, particularly in the HYD-prepared samples, achieving an adsorption capacity of 2.33 mg per g Fe by creating stable Cr-adsorbed species. X-ray photoelectron spectroscopy (XPS) and X-ray absorption spectroscopy (XAS) confirmed the Cr species adsorbed on Fe/Z_HYD, identifying ion-exchange lattice structures of $Fe_{3-x}Cr_xO_4$ and $Fe_{1-x}CrOOH$ as the most stable forms. This study provides insights into the potential of Fe_3O_4/ZSM-5 zeolite for Cr(VI) remediation.

Received 22nd September 2024
Accepted 29th January 2025

DOI: 10.1039/d4ra06845a

rsc.li/rsc-advances

1. Introduction

Chromium (Cr) is a primary metal pollutant that contaminates water and wastewater. In the environment, chromium exists in both the Cr(III) and Cr(VI) oxidation states. Cr(VI) is more toxic and carcinogenic,[1,2] whereas Cr(III) is a main component of living organisms. Therefore, the reduction of Cr(VI) to Cr(III) has attracted great attention. Various methods have been employed for detoxifying Cr(VI), including ferrous reduction, electrochemical reduction, and bioreduction.[3–5] However, these methods are complicated and require additional processes for further treatment. Additionally, electrochemical reduction and bioreduction are associated with high operating costs. As a result, researchers are seeking a method that is simple, low-cost, and readily available. One promising method of interest is adsorption using materials with redox properties.

Magnetite (Fe_3O_4) containing both Fe(II) and Fe(III) is an interesting adsorbent due to its suitable redox potential and excellent magnetic properties, which affect separation, chemical stability, and non-toxicity.[6,7] The adsorption of Cr(VI) by magnetite has received much attention from researchers for removing Cr(VI) from water.[8–10] In the adsorption process, the surface area of the adsorbent is important. Magnetite nanoparticles synthesized *via* the co-precipitation method have a spherical shape and a particle size of 10–15 nm, with an adsorption capacity of 3.56 mg g^{-1}.[11] Mesoporous magnetite nanospheres with hollow interiors were synthesized by the solvothermal method, providing spherical shapes ranging from 150–250 nm in diameter and having an adsorption capacity of 6.64 mg g^{-1}.[12] Recently, the synthesis methods for Fe_3O_4 have been found to affect the size, shape, and adsorption capacity. However, the problem of coaggregation of the magnetic nanoparticles decreases the effective surface area of nanoparticles, thus reducing their reactivity. In addition, the Cr-adsorbed species created on the Fe_3O_4 adsorbent were reported as crucial rows in their adsorption ability. Senamart *et al.* reported that the formation of stable Cr^{3+} in $Fe_{1-x}Cr_xOOH$ and $Fe_{3-x}Cr_xO_4$, through the adsorption of Cr onto Fe_3O_4, improved the adsorption capacity.[13] The stable form of Cr^{3+} on Fe_3O_4 is strongly attached to the surface, typically through chemical

[a]*Materials Chemistry Research Center, Department of Chemistry, Faculty of Science, Khon Kaen University, Khon Kaen 40002, Thailand. E-mail: sirilo@kku.ac.th*
[b]*School of Chemistry, Institute of Science, Suranaree University of Technology, Nakhon Ratchasima 30000, Thailand*

† Electronic supplementary information (ESI) available. See DOI: https://doi.org/10.1039/d4ra06845a

bonding. This robust bonding improves the adsorption efficiency by preventing Cr^{3+} from desorbing, ensuring long-term stability in the system.

To reduce coaggregation, the dispersion of Fe_3O_4 on zeolite porous material is important. Mai *et al.*[14] developed a zeolite NaA/Fe_3O_4 composite derived from rice husk ash for the removal of Cr(VI) from water, achieving a maximum adsorption capacity of 69.23%. Additionally, the magnetic Fe_3O_4/zeolite composites were reported to have high performance in removing toxic compounds, including dyes and organic molecules.[15,16] Zeolites are often used as supports or stabilizers for metal catalysts due to their unique microporous structures and ion-exchange properties.[17] These characteristics can help to disperse metal nanoparticles and reduce aggregation, although this is not always guaranteed under certain conditions. The aggregation of metal particles, especially when dispersed in liquids or during catalytic reactions and adsorption, is influenced by several factors. These factors include the size of the metal particles, the surface chemistry, the porosity of the zeolite, and the interactions between the metal and the zeolite surface.[18] Research indicates that certain design considerations are essential for zeolites to effectively stabilize metal dispersions and prevent aggregation, as discussed by Wang *et al.*[19] Metal ions were initially grafted onto the zeolite surface using ultrasonication, followed by a seed-assisted secondary growth method. The results demonstrated good metal dispersion and stability during a catalytic reaction. Thus, zeolites have the potential to decrease aggregation in metal dispersions, their effectiveness depends on careful design and engineering of both the zeolite structure and the metal dispersion process. Incorporating Fe_3O_4 into the ZSM-5 zeolite framework is an effective strategy to enhance the catalytic properties of ZSM-5. This approach introduces magnetic properties and improves the dispersion and stabilization of metal species. Fe_3O_4 nanoparticles can be synthesized either within the ZSM-5 framework or on its surface, achieved through direct incorporation during the zeolite synthesis or through post-synthesis modification.[20] The direct synthesis or *in situ* incorporation of Fe_3O_4 within the ZSM-5 framework can be achieved by adding iron precursors, such as iron salts, to the hydrothermal synthesis mixture of ZSM-5. During the crystallization process, Fe^{3+} ions are incorporated into the zeolite structure, leading to the formation of Fe_3O_4 nanoparticles embedded within the framework.[21] The even shape and size distribution of metal oxide within the zeolite enhances stability and catalytic activity. It also reduces leaching or aggregation, which can occur during post-synthesis processes such as co-precipitation method.

This study focused on synthesizing magnetite (Fe_3O_4) and magnetite-supported ZSM-5 zeolite using co-precipitation (COP) and hydrothermal (HYD) methods. We investigated the adsorption performance of hexavalent chromium (Cr(VI)) and the capability of these adsorbents to reduce Cr(VI) into more stable forms. The experimental design aimed to explore the relationship between the structures and dispersion of Fe_3O_4 in the adsorbents, both *in situ* (HYD) and post-synthesis (COP), concerning their adsorption capacity and reduction ability. X-ray absorption spectroscopy (XAS) and X-ray photoelectron spectroscopy (XPS) were utilized to investigate the local structure of iron (Fe) in the materials and the surface characteristics of the adsorbents. The understanding of Fe_3O_4 interactions within the materials, and its influence in the adsorption and reduction processes for Cr(VI) were investigated.

2. Materials and methods

2.1. Materials

Silicon and aluminum sources were silica (SiO_2) (Merck) and sodium aluminate ($NaAlO_2$) (Sigma-Aldrich). Fe(II) and Fe(III) precursors were ferrous sulfate ($FeSO_4 \cdot 7H_2O$, Carlo Erba) and iron(III) chloride ($FeCl_3$, ACROS). Potassium dichromate ($K_2Cr_2O_7$) and sodium acetate (NaOAc) were obtained from LOBA. Potassium hydroxide pellet (KOH), hydrochloric acid 38% (HCl) and ethylene glycol (EG) were purchased from QRëC™. 1,5-Diphenylcarbazide was purchased from Merck and sodium hydroxide (NaOH) was purchased from RCI Labscan.

2.2. Synthesis of HZSM-5 zeolite by hydrothermal method

The NaZSM-5 zeolite was synthesized using a hydrothermal method. First, a sodium silicate (Na_2SiO_3) solution was prepared by dissolving 17.28 g of SiO_2 in 11.87 g of NaOH in 40 mL DI water. Then, a solution of 0.74 g of $NaAlO_2$ dissolved in 25 mL DI water was added dropwise to the Na_2SiO_3 solution while stirring magnetically. The pH of the mixture was adjusted to around 11 by adding 1 M H_2SO_4 (approximated volume 125–130 mL) to obtain zeolite gel. The gel was then crystallized in a Teflon-lined autoclave at 170 °C for 72 hours. The solid product was centrifuged and neutralized by washing with DI water. The as-synthesized powder was dried at 110 °C for 12 hours and then calcined at 550 °C for 5 hours to obtain NaZSM-5 zeolite. Subsequently, 1 gram of NaZSM-5 was ion-exchanged with 30 mL of 1.25 M ammonium carbonate ($(NH_4)_2CO_3$) under reflux conditions at 80 °C for 6 hours. After the ion exchange procedure, the ammonium form (NH_4-ZSM-5) was washed with DI water and dried at 110 °C for 12 hours. The proton form of ZSM-5 (HZSM-5) was obtained after calcination at 400 °C for 4 hours.

2.3. Synthesis of Fe_3O_4 and Fe_3O_4/ZSM-5 *via* hydrothermal method

The hydrothermal Fe_3O_4, namely Fe_HYD, was synthesized using the following procedure reported in the literature.[22] The 1.94 g of $FeCl_3$ precursor was dissolved in a mixture of 40 mL ethylene glycol (EG) in a two-necked round-bottom flask under N_2 atmosphere. The mixture was stirred for 30 min before adding 10 mL of 1.2 M sodium acetate and continuously stirred for 3 h. Then, the mixture was transferred to a Teflon-lined autoclave and crystallized at 190 °C for 24 h. The obtained product was washed with DI water and dried at 50 °C overnight.

The synthesis of Fe_3O_4 supported on HZSM-5 zeolite using a hydrothermal method, namely Fe/Z_HYD, was performed using a similar procedure to Fe_HYD. The 0.5 g HZSM-5 powder was added to the $FeCl_3$ solution before a crystallization step. To investigate the effect of Fe-loading on adsorption efficiency,

appropriate amounts of iron precursors were utilized to prepare Fe/ZSM-5 with Si/Fe ratios of 1.1, 1.5, and 3.5.

2.4. Synthesis of Fe_3O_4 and Fe_3O_4/ZSM-5 *via* co-precipitation method

The co-precipitated Fe_3O_4 namely Fe_COP was synthesized following the methodology described below.[23] The mixture of 0.4 M $FeCl_3$ (20 mL) and 0.2 M $FeSO_4 \cdot 7H_2O$ (20 mL) were prepared. The Fe_3O_4 powder was obtained after adjusting the solution to a pH of about 10–11 by using NaOH and continuously stirring for 1 h to complete precipitation. The obtained powder was washed with DI water and dried at 50 °C overnight.

The co-precipitated Fe_3O_4 supported on HZSM-5 labeled Fe/Z_COP was prepared similarly to the co-precipitation method of Fe_COP. The 0.5 g of HZSM-5 was added to the mixture of iron solution before adjusting pH. The obtained powder was washed and dried at 50 °C overnight.

2.5. Characterization

The crystalline structures of the synthesized materials were confirmed by the Powder X-ray Diffractometer (XRD), PANalytical, EMPYREAN. Structural confirmations of the materials were determined couple with using the Fourier-Transform Infrared Spectrometer (FT-IR), Bruker in TENSOR27 model. The morphologies and dispersion of the samples were investigated by Transmission Electron Microscope (TEM), Tecnai G^2, FEI and Scanning Electron Microscope (SEM), QUANTA 450, FEI. The oxidation state and speciation of the iron species were determined by X-ray adsorption spectroscopy (XAS) and provided at BL1.1W, Synchrotron Light Research Institute (SLRI) in the intermediate photon energy range of 5.7–6.7 keV and 7.0–8.0 keV for Cr K-edge and Fe K-edge, respectively. The chemical states of Fe Cr and O were analyzed using X-ray photoelectron spectroscopy (XPS), PHI 5000 VersaProbe II, ULVAC-PHI, Japan at BL 5.3, the SUT-NANOTEC-SLRI Joint Research Facility, Synchrotron Light Research Institute, Thailand.

2.6. Cr(VI) adsorption in water

The 100 ppm Cr(VI) stock solution was primarily prepared by dissolving 0.0282 g of $K_2Cr_2O_7$ in 100 mL DI water. All working solutions at the desired concentration were prepared by diluting the stock solution with DI water. The adsorption experiments were carried out in a flask by introducing 0.02 g of adsorbent into 50 mL of Cr(VI) solution concentration of 1 ppm. The effects of pH, contact time and temperature were studied. The pH of the mixture was adjusted in the range 2–4 by 0.1 M HCl and 0.1 M NaOH to modulate the surface charge of adsorbents, the degree of ionization, and the species of adsorbate.[24,25] The effect of contact time was carried out at 10, 30, 60 and 90 minutes. For the thermodynamic study, the temperature was varied at 30 °C, 45 °C, and 60 °C. The adsorbent was separated by an external magnet after the adsorption process. The filtrate solution was taken and Cr(VI) concentrations were determined by the colorimetric method.[26,27] The complexation of Cr(VI) supernatant and 1,5-diphenylcarbazide ligand was performed under pH ~ 2 adjusting by 10% (v/v) H_2SO_4. The solution was provided violet-red color then analyzed by UV-visible spectrometry at $\lambda = 540$ nm. The adsorption capacity of Cr (mg per g Fe) was calculated by the following equation.

$$\text{Adsorption capacity } (q_e) = \frac{(C_0 - C_e)}{W} V$$

where C_0 and C_e (mg L^{-1}) are the initial and equilibrium metal concentration, respectively, V (L) is the solution volume and W (g) is adsorbent weight.

After adsorption experiment, the local structures and species of Fe and Cr on the adsorbent surfaces were investigated by using X-ray absorption (XAS) and X-ray photoelectron spectroscopy (XPS) techniques.

3. Results and discussion

3.1. Structural characterization by XRD

The XRD patterns of Fe_3O_4 crystalline prepared by hydrothermal and co-precipitation methods (Fig. 1a) show cubic

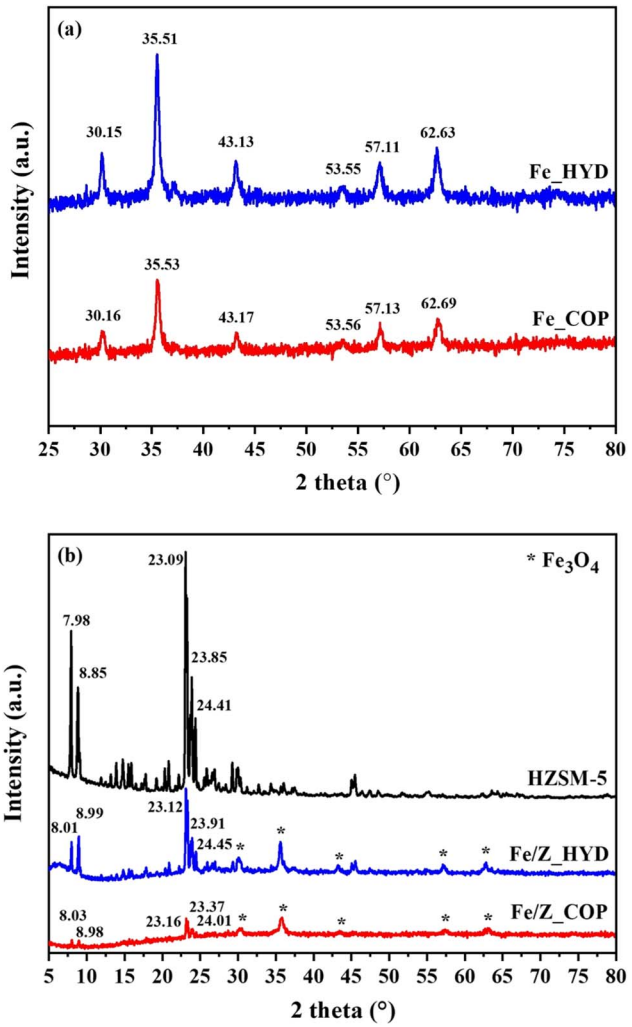

Fig. 1 XRD patterns of Fe_HYD, Fe_COP (a) and Fe/Z_HYD, Fe/Z_COP (b).

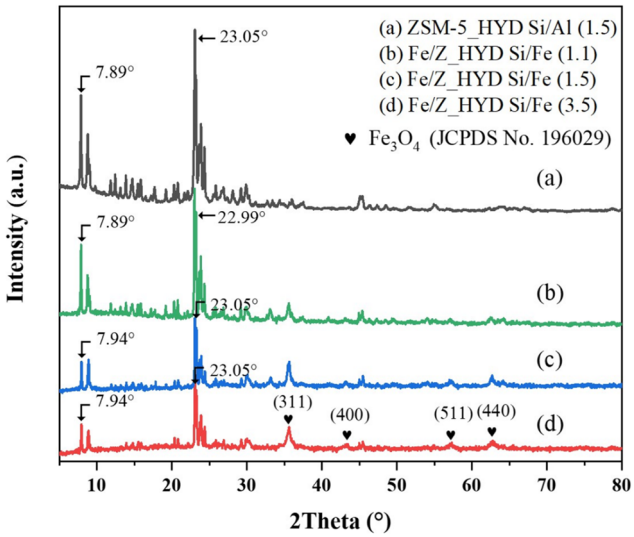

Fig. 2 XRD patterns of Fe/ZSM-5 with varying Fe loading compared with a bare ZSM-5.

structures corresponding to the JCPDS no. 19-0629 database.[8] The characteristic plane of (220), (311), (400), (422), (511), (440) are observed at 2θ = 30.16°, 35.53°, 43.17°, 53.56°, 57.13°, 62.69°, respectively. However, the main peak positions of Fe_COP are systematically shifted to higher values and peak broadening than Fe_HYD. These results indicated the presence of lower crystallinity or short-range order phases of the Fe_xO_y nanoclusters on the Fe_COP sample. The samples of Fe/Z_HYD and Fe/Z_COP are plotted to compare with the pristine HZSM-5 as shown in Fig. 1b. The characteristic peaks of HZSM-5 (ref. 28 and 29) are observed after Fe_3O_4 supporting by two methods with no significant shift of the peak positions. The peak intensities of the Fe/Z_HYD zeolite were significantly lower than those of the pristine HZSM-5. This decrease may be attributed to the desilication of the zeolite framework that occurred during the precipitation of Fe_3O_4 in a strong alkaline solution, which resulted in partial deconstruction of the zeolite crystalline structure.

The XRD patterns of Fe/ZSM-5_HYD with varying iron loadings are presented in Fig. 2. The crystal structure of ZSM-5 remained stable through all Fe loading amounts. The characteristic peaks corresponding to the Fe_3O_4 phase were observed on all samples. Notably, the iron loading impacted the structural distortion of the zeolite framework. In samples with low iron content, specifically those with Si/Fe ratios of 1.5 and 3.5, the reflection corresponding to the (101) plane at 7.94° shifted slightly to a higher 2θ compared to the bare ZSM-5. This shift

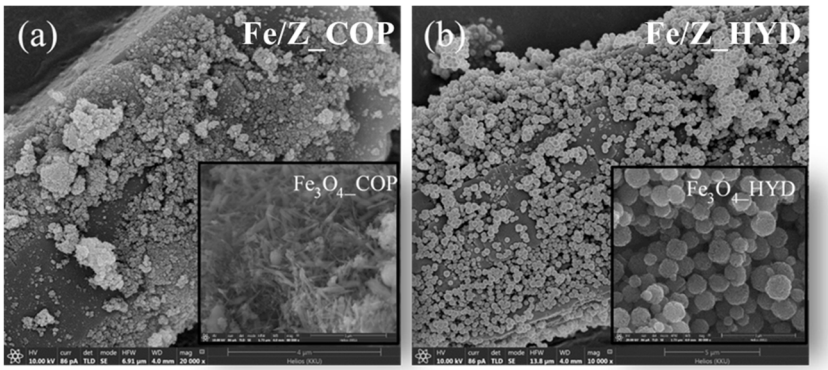

Fig. 3 SEM images of the Fe/Z_COP (a) include Fe_3O_4_COP (inset) and the Fe/Z_HYD (b) include Fe_3O_4_HYD (inset).

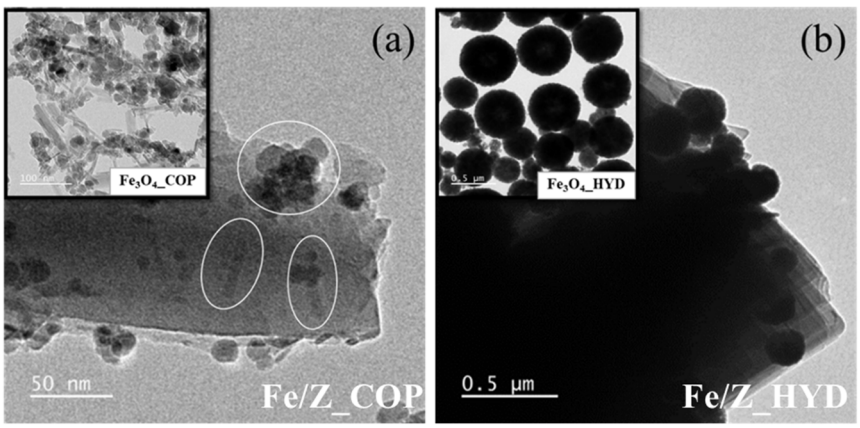

Fig. 4 TEM images of the Fe/Z_COP (a) include Fe_3O_4_COP (inset) and the Fe/Z_HYD (b) include Fe_3O_4_HYD (inset).

suggests a contraction in the *d*-spacing, which may be attributed to the partial incorporation of Fe^{3+} into the zeolite framework.[30] In contrast, the sample with high iron content, with a Si/Fe ratio of 1.1, showed a slight shift to a lower 2θ for the (501) plane at 22.09°, suggesting an expansion of the *d*-spacing in the ZSM-5 structure at high iron loading. These results are consistent with SEM mapping, which revealed the presence of large, separated iron oxide particles distinct from the ZSM-5 framework.

3.2. Morphologies and physical properties of the adsorbents

3.2.1 SEM and TEM. The materials were characterized using SEM and TEM images, as depicted in Fig. 3 and 4. SEM images of Fe_COP and Fe/Z_COP (Fig. 3a) showed a mixed phase of rod-like and granular structures of Fe_3O_4 dispersed on ZSM-5 support. Nanorod morphology of Fe_3O_4 has also been reported in the literature.[31] The Fe_3O_4 structure could be transformed from β-FeOOH, which is formed as an intermediate during the precipitation process. Additionally, uniform

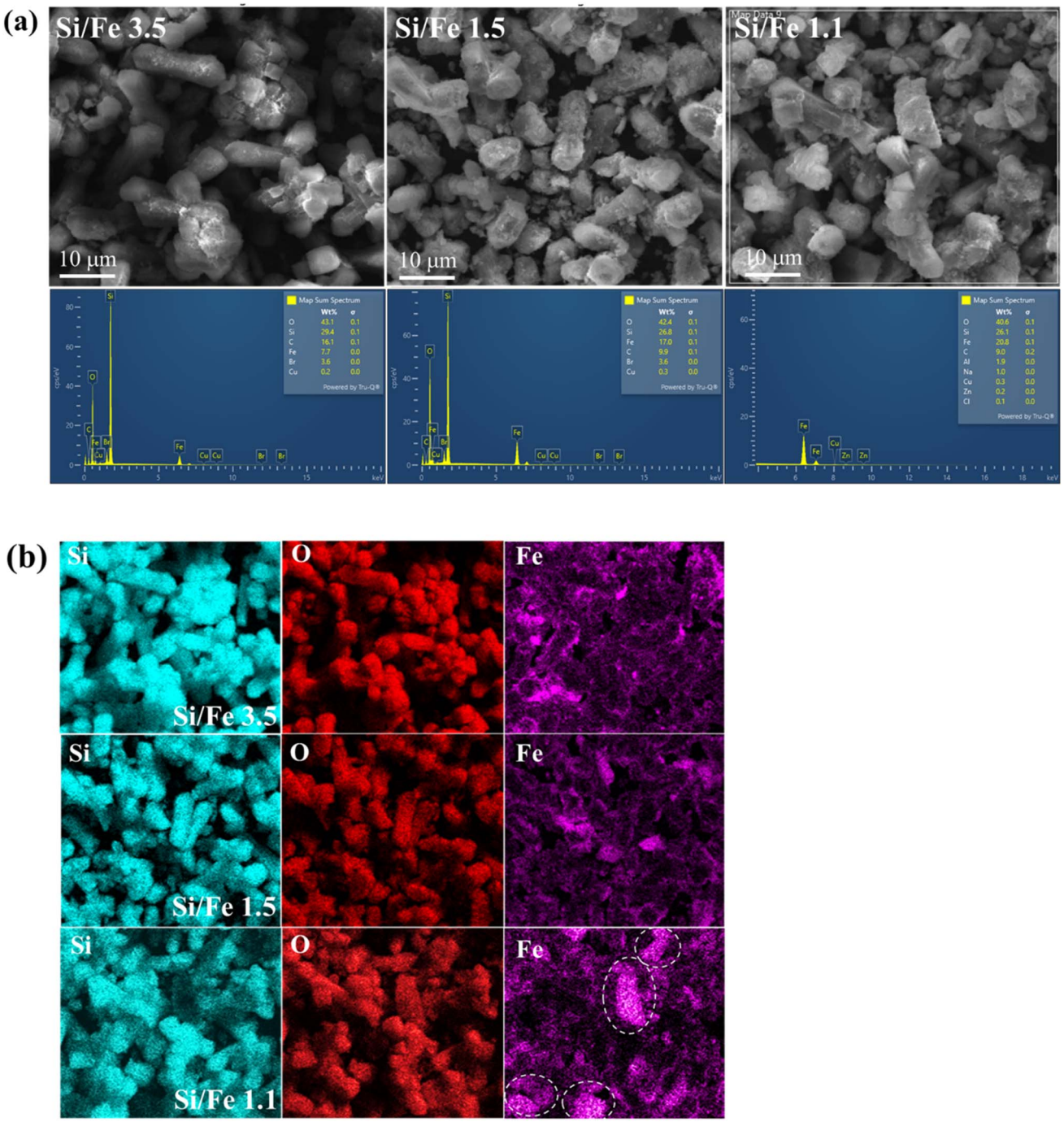

Fig. 5 SEM images and element percentages (a) and element distribution (b) of Fe/ZSM-5_HYD with varying Fe loading.

spherical particles of Fe_3O_4 with good dispersion on the zeolite support were observed in Fe_HYD and Fe/Z_HYD (Fig. 3b). The particle sizes of Fe_3O_4 dispersed on zeolite supports were determined using TEM images. Spherical Fe_3O_4 particles on Fe_HYD and Fe/Z_HYD had an average diameter of 400–500 nm (Fig. 4b). On the other hand, the particle size of rod-like and granular Fe_3O_4 on Fe_COP and Fe/Z_COP was about 20–50 nm (Fig. 4a). These results indicate that the synthesis method influences the shape and size of the Fe_3O_4 particles dispersed on the zeolite support.

The particle sizes of Fe/ZSM-5_HYD remained consistent despite variations in iron (Fe) content. Energy Dispersive Spectroscopy (EDS) analysis revealed that the atomic percentage of Fe increased with higher iron loading. The average Si/Fe ratios determined by the SEM-EDS technique were 3.5, 1.5, and 1.1, as shown in Fig. 5a. An illustration of the iron distribution on the support is presented in Fig. 5b. The results demonstrated that particle aggregation occurred as Fe loading increased. A significant iron oxide particle was observed in the Fe/ZSM-5 sample with a Si/Fe ratio of 1.1.

3.2.2 N_2 adsorption–desorption. The surface area and pore analysis of the adsorbents in Table 1 were determined based on the N_2 adsorption–sorption isotherms shown in Fig. 6. The adsorption isotherms were relevant to the preparation methods of the adsorbents. The adsorption isotherms for all samples exhibited IUPAC type I, indicating a microporous structure. However, a hysteresis loop was also observed within a broad P/P_0 range of 0.4–0.9 for all adsorbents. These findings suggested the presence of a pore size distribution attributed to the interparticle interactions of the Fe_3O_4 coating on the zeolite surface. Notably, a pronounced and significant volume of the hysteresis loop for Fe_COP and Fe/Z_COP in the P/P_0 range of 0.6–0.9, corresponding to hysteresis H1 type, was recorded. This result correlates well with the rod-like shape of the Fe_3O_4 particles seen in SEM images, which may facilitate the formation of cylindrical interparticle pores. The surface area of Fe_COP was greater than that of Fe_HYD, which correlates with the larger size of Fe_HYD as observed in SEM and TEM images. A significant improvement in the surface areas of the supported Fe_3O_4 adsorbents was noted, attributed to the high surface area of the zeolite. Additionally, the surface area of Fe/Z_HYD exceeded that of Fe/Z_COP due to the better dispersion of the Fe_3O_4 particles.

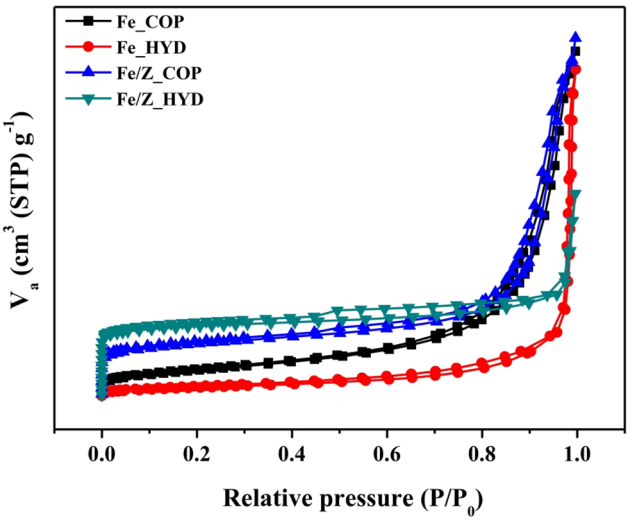

Fig. 6 N_2 adsorption–desorption isotherms of the adsorbents.

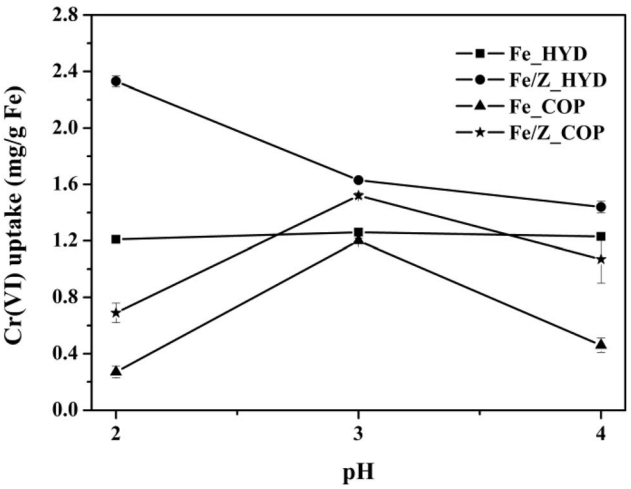

Fig. 7 Effect of pH to the adsorption capacity of all samples (condition: Cr(VI) initial concentration = 1 ppm, time = 30 min. and temperature 30 °C).

3.3. Cr(VI) adsorption ability

3.3.1 Effect of pH. The pH at which adsorption takes place can affect both adsorbate and adsorbent, which in turn affects

Table 1 Surface properties of the iron oxide materials analyzed by N_2 adsorption–desorption analysis and Fe content in 1 g sample by AAS analysis[a]

Sample	Surface area ($m^2\ g^{-1}$)**	Pore volume ($cm^3\ g^{-1}$)*	Average pore diameter (nm)*	Fe content by AAS ($g\ g_{sample}^{-1}$)
Fe_COP	85	0.42	11	0.78
Fe_HYD	34	0.35	9	0.89
Fe/Z_COP	165	0.39	25	0.50
Fe/Z_HYD	232	0.14	2	0.22
Bare ZSM-5	239	0.11	3	

[a] *Calculated by BJH, ** calculated by BET.

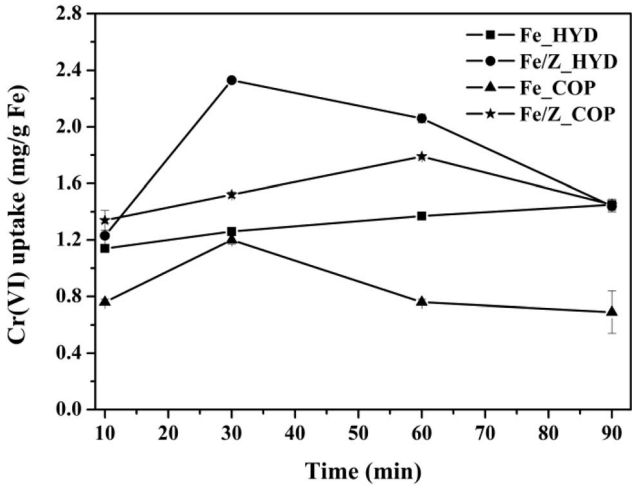

Fig. 8 Effect of contact time to the adsorption capacity of all samples (condition: Cr(VI) initial concentration = 1 ppm, pH 2 for Fe/Z_HYD, pH 3 for F_HYD, Fe_COP, Fe/Z_COP and temperature 30 °C).

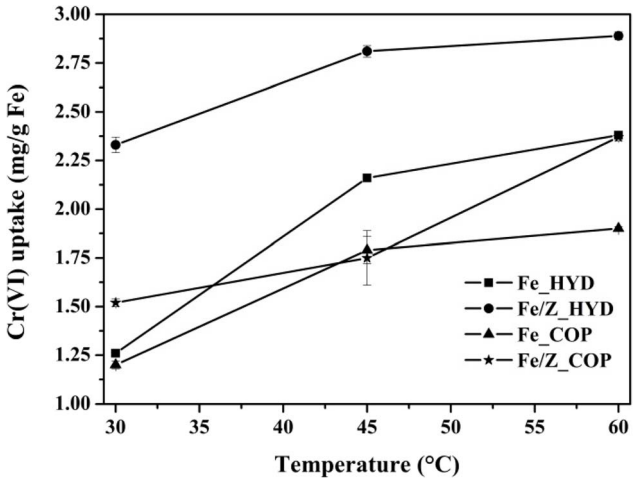

Fig. 9 Effect of temperature to the adsorption capacity of all samples (condition: Cr(VI) initial concentration = 1 ppm, pH 2 for Fe/Z_HYD, pH 3 for F_HYD, Fe_COP, Fe/Z_COP and time 30 min).

the adsorption capacity as shown in Fig. 7. We studied the optimal pH for adsorption and found that Fe_COP and Fe/Z_COP had the highest capacity for Cr(VI) at pH 3, while Fe/Z_HYD had the highest capacity at pH 2. The solution pH did not significantly affect the adsorption capacity of Fe_HYD. The different adsorption behaviors were attributed to the iron oxide structures present in the adsorbents. The surface zeta potential (isoelectric point or pH_{pzc}) of Fe_3O_4 occurs at a pH of 3.0–4.0.[32] Below the isoelectric point, the hydroxyl groups of –FeOH on the surface change to functional groups of $-FeOH_2^+$ due to protonation. In the pH range of 2.0–6.5, Cr(VI) primarily exists in the form of $HCrO_4^-$. Therefore, at pH < pH_{pzc}, strong attraction between $-FeOH_2^+$ and $HCrO_4^-$ occurs *via* electrostatic adsorption. The highest surface protonation of Fe_3O_4 at pH 2 led to the maximum adsorption capacity of Fe/Z_HYD. The result is attributed to the effective dispersion of Fe_3O_4 particles on the zeolite support, as found in the SEM image.

3.3.2 Effect of time. The study investigated the impact of contact time on the adsorption capacity of Cr(VI) at 10, 30, 60, and 90 minute intervals, as depicted in Fig. 8. The results indicated that the adsorption capacity of the adsorbent was influenced by the contact time. Fe/Z_HYD and Fe_COP reached their maximum capacities at 30 minutes, while Fe/Z_COP and Fe_HYD reached their maximum capacities at 60 minutes. The adsorption saturation time may be related to the availability of active sites on the adsorbents. Subsequently, there was a slight decrease in Cr(VI) uptake over time, attributed to repulsive forces between the solute molecules on the solid surface and in the bulk liquid phase.[33]

3.3.3 Effect of temperature. The effect of temperature on the adsorption capacity is illustrated in Fig. 9. The uptake of Cr(VI) increases with increasing temperature for all samples, indicating that the adsorption process is endothermic. These findings are supported by thermodynamic calculations. The adsorption thermodynamic study was conducted at 30 °C, 45 °C, and 60 °C using a 1 ppm Cr(VI) solution and 0.02 g of adsorbents. The thermodynamic parameters are listed in Table 2. All adsorbents showed similar results. They exhibited a positive standard enthalpy change ($\Delta H°$), indicating an endothermic adsorption behavior.[34] In addition, the $\Delta H°$ is lower than 40 kJ mol^{-1}, revealing physisorption behavior.[35] The adsorptions were shown to be feasible and the spontaneous nature of adsorption was confirmed by the Gibbs free energy changes ($\Delta G°$).[36] The positive entropy change ($\Delta S°$) of Fe_HYD, Fe/Z_HYD, Fe_COP, and Fe/Z_COP indicated indicates an increase in disorder at the solid–liquid interface involving the adsorbent surface and the Cr(VI) solutions.[37,38]

3.3.4 Effect of Fe loading. The chromium (Cr) adsorption capacity of Fe/ZSM-5 over time was investigated with varying levels of iron loading, illustrated in Fig. 10. The maximum adsorption capacities for Cr on Fe/ZSM-5 were ranked as follows: Si/Fe ratio of 1.5 > 3.5 > 1.1. The study demonstrated that iron oxide agglomeration negatively impacted its

Table 2 Thermodynamic parameters of all samples

Materials	$\Delta H°$ (kJ mol^{-1})	$\Delta S°$ (J mol^{-1} K^{-1})	$\Delta G°_{303}$ (kJ mol^{-1})	$\Delta G°_{313}$ (kJ mol^{-1})	$\Delta G°_{333}$ (kJ mol^{-1})
Fe_COP	23.99	87.29	−2.46	−3.77	−5.08
Fe_HYD	31.18	113.40	−3.18	−4.88	−6.58
Fe/Z_COP	15.97	59.59	−2.08	−2.98	−3.87
Fe/Z_HYD	7.78	36.49	−3.28	−3.82	−4.37

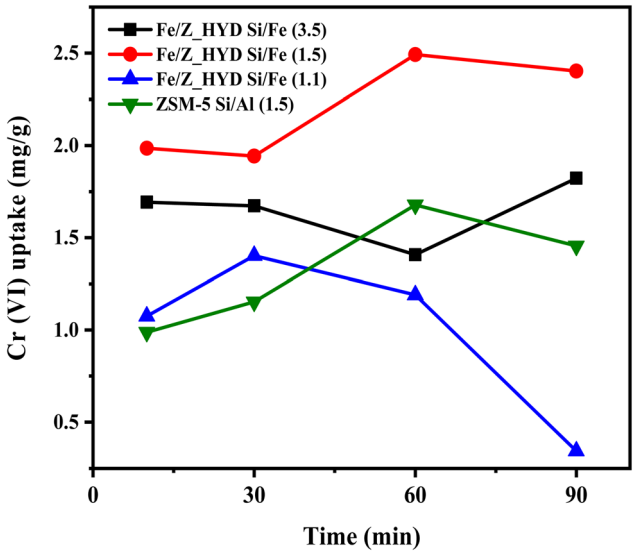

Fig. 10 Cr uptake over time for Fe/ZSM-5_HYD with varying Fe loading compared to bare ZSM-5 under conditions of 0.02 g adsorbent and 50 mL of 1 ppm Cr(VI) solution.

adsorption capacity, particularly in Fe/ZSM-5, with a Si/Fe ratio of 1.1. Notably, the bare ZSM-5 with a Si/Al ratio of 1.5 showed the lowest adsorption capacity after 30 minutes. The adsorption behavior of bare ZSM-5 closely resembled that of Fe/ZSM-5 with a Si/Fe ratio of 1.5. These results indicate that incorporating iron into ZSM-5 enhances its efficiency in chromium adsorption.

3.4. Cr(VI) reduction on solid adsorbents

3.4.1 Surface analysis of Fe 2p and O 1s XPS. The XPS analysis of Fe 2p and O 1s energies of the synthesized adsorbents in Fig. 11 and S1† indicated the typical Fe_3O_4 structure. However, the Fe 2p and satellite energies of the Fe_COP adsorbent were slightly higher than those of the other samples, suggesting the dominance of the Fe^{3+} component in the Fe_3O_4 structure. The O 1s energies found in the pristine samples were assigned to the lattice oxygen of Fe–O and the adsorbed hydroxyl group of Fe–OH at 530.6 (0.2) and 532.5 (0.4) eV, respectively.[39–41] The zeolite support had no significant influence on the surface-iron species in the pristine samples. After Cr adsorption, the Fe 2p and O 1s energies of Cr@Fe_COP, Cr@Fe_HYD, and Cr@Fe/Z_COP shifted to lower energies than the pristine samples. This shift indicated an increase in Fe^{2+} species in the samples after Cr adsorption. It was proposed that the electrostatic adsorption of $Fe_2O_3{\cdot}Fe^{2+}O{\cdot}(HCrO_4)$ could result in the formation of possible species. Additionally, in all adsorbed samples, the O 1s energies corresponding to the lattice hydroxyl group of Fe–OH were observed at 533.5 (0.3) eV, indicating the formation of the FeOOH species through Cr^{6+} adsorption in an acidic solution (H^+) to form $Fe_{(1-x)}Cr_xOOH(s)$ as shown in eqn (1)–(3), which contained the reduced Cr^{3+} species.[13,27,40,41] The finding of Fe^{3+} and Cr^{3+} species on the adsorbent surfaces indicates that a reduction of Cr^{6+} to Cr^{3+} simultaneously occurred through adsorption. On the other hand, the Fe 2p and O 1s energies determined in Cr@Fe/Z_HYD were slightly higher than those of the pristine Fe/Z_HYD. The finding represented a strong Fe^{3+} and O^{2-}/OH^- interaction in lattice sites after Cr-adsorption. The dominant species is probably explained by eqn (4).[13] The Cr^{6+} was reduced to Cr^{3+} by FeO in the Fe_3O_4 ($FeO{\cdot}Fe_2O_3$) structure. $Fe_{3-x}Cr_xO_4$ (or $FeO{\cdot}Cr_2O_3$) containing Fe^{2+} and Cr^{3+} species could be formed and strongly adsorbed on the outer surface of Fe_3O_4.

$$H_2CrO_4 \rightarrow HCrO_4^- + H^+ \quad (1)$$

$$2HCrO_4^- + 2Fe^{2+} + 10H^+ \rightarrow 2Fe^{3+} + 2Cr^{3+} + 6H_2O + O_2 \quad (2)$$

$$(1-x)Fe^{3+} + (x)Cr^{3+} + 2H_2O \rightarrow Fe_{(1-x)}Cr_xOOH(s) + 3H^+ \quad (3)$$

$$2FeO + 4HCrO_4^- + 4H^+ \rightarrow 2Fe_{(3-x)}Cr_xO_4 + 4H_2O + 3O_2 \quad (4)$$

3.4.2 Bulk analysis by XAS

3.4.2.1 Fe K-edge XANES. The analysis of the bare and Cr-adsorbed materials was performed using XANES of Fe K-edge energy, as shown in Fig. 12a and c. The pre-edge and edge energies of Fe XANES spectra were not significantly shifted by Cr-adsorption. The proportions of Fe^{2+} and Fe^{3+} in the Fe_3O_4 samples were further investigated using a Linear Combination Fit (LCF) in the Athena program, comparing with Fe_3O_4 (Fe^{2+}/Fe^{3+}) and Fe_2O_3 (Fe^{3+}) standards, as depicted in Fig. 12b and d. The Fe_3O_4 content in the samples of bare Fe_HYD, Fe/Z_COP, and Fe/Z_HYD ranged from 80% to 87%. In contrast, the Fe_COP sample showed approximately 62% Fe_3O_4 content. This indicates that the zeolite support enhances the formation of the Fe_3O_4 major phase through the co-precipitation method. After the adsorption of Cr(VI), there was a significant decrease in the Fe_3O_4 content of the adsorbed samples: Cr@Fe_COP, Cr@Fe_HYD, and Cr@Fe/Z_COP. These reductions were about 20–25% when compared to their bare counterparts. Additionally, the percentage of the Fe_2O_3 component showed an increase. These results confirm that Cr^{6+} was reduced to Cr^{3+} by Fe^{2+} within the Fe_3O_4 structure. Notably, the Fe_3O_4 content in Cr@Fe/Z_HYD decreased by approximately 31%, which aligns well with the maximum adsorption capacity of Cr(VI) reported in Section 4.3.

3.4.2.2 Fe L-edge XANES. To investigate the phase transformation of iron, Fe $L_{2,3}$-edge XANES spectroscopy was utilized. The speciation of iron could be elucidated by the shape of the Fe L_3-edge peak, with further peak splitting resulting from the relation of crystal field splitting of Fe 3d orbitals and electronic interactions. In a standard Fe_2O_3, Fe ions occupy the same octahedral sites close to perfect O_h symmetry, resulting in a well-defined spectrum pattern with a clear splitting at the L_3-edge. In contrast, Fe ions in Fe_3O_4 involve three different local structures: Fe(II) octahedral, Fe(III) octahedral, and Fe(III) tetrahedral. Consequently, the summation of these three different local components reduces the splitting resolution of peaks A and B in Fe_3O_4.[42] Similar to the XANES spectra in Fig. 13, the A–B peak splitting in Fe_HYD and Fe/Z_HYD was less than that of Fe_COP and Fe/Z_COP. The results indicate

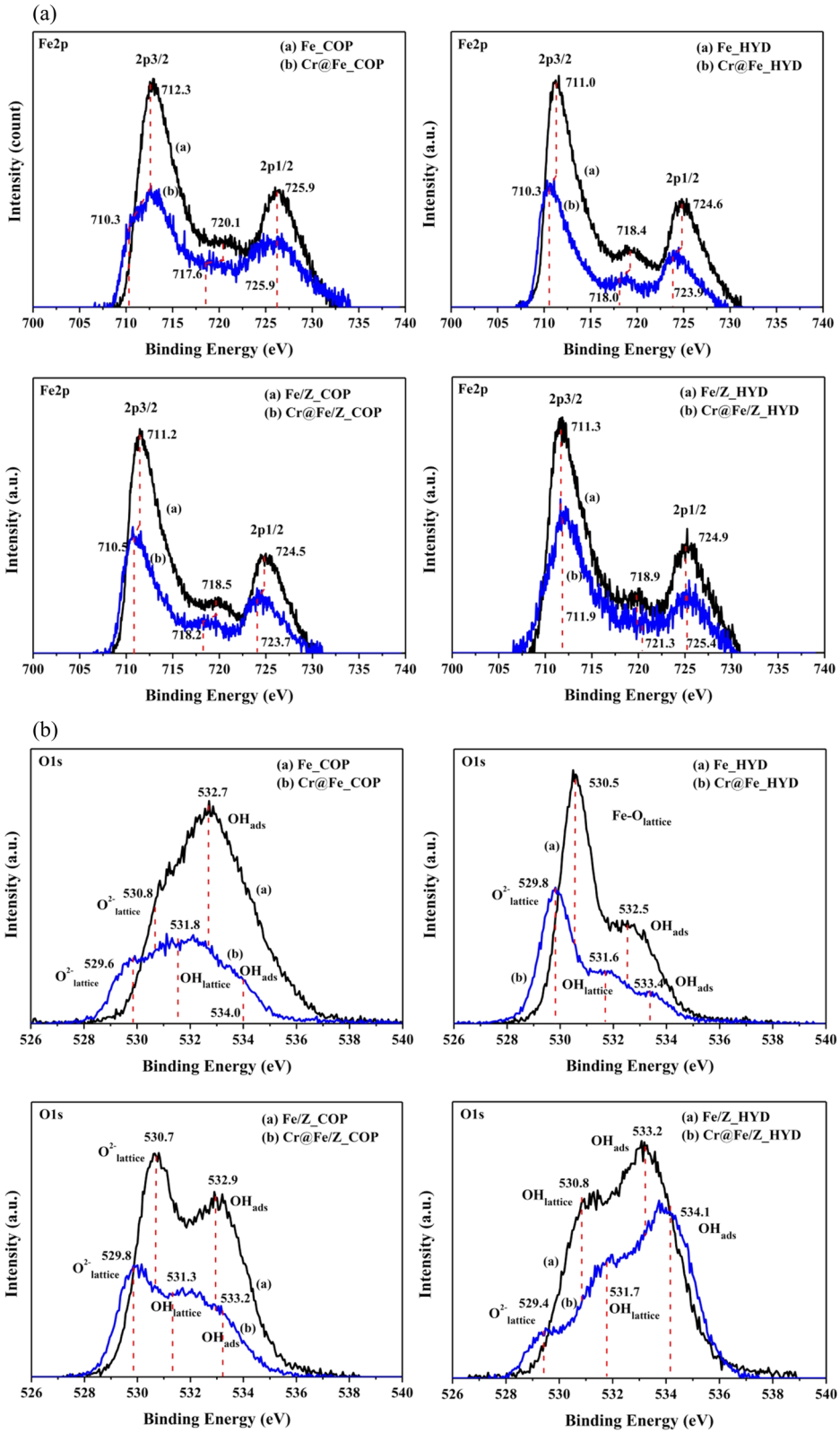

Fig. 11 XPS Fe 2p (a) and O 1s (b) spectra of the bare and Cr-adsorbed samples.

a tendency to observe a higher Fe_2O_3 content using the COP method, which was not clearly defined in the Fe K-edge XANES analysis. The A–B splitting in Cr@Fe_COP and Cr@Fe/Z_COP showed a clear increase in the intensity of the A peak after Cr-adsorption compared to the bare absorbent. This indicates the transformation of Fe_3O_4 to Fe_2O_3 structure due to Cr-

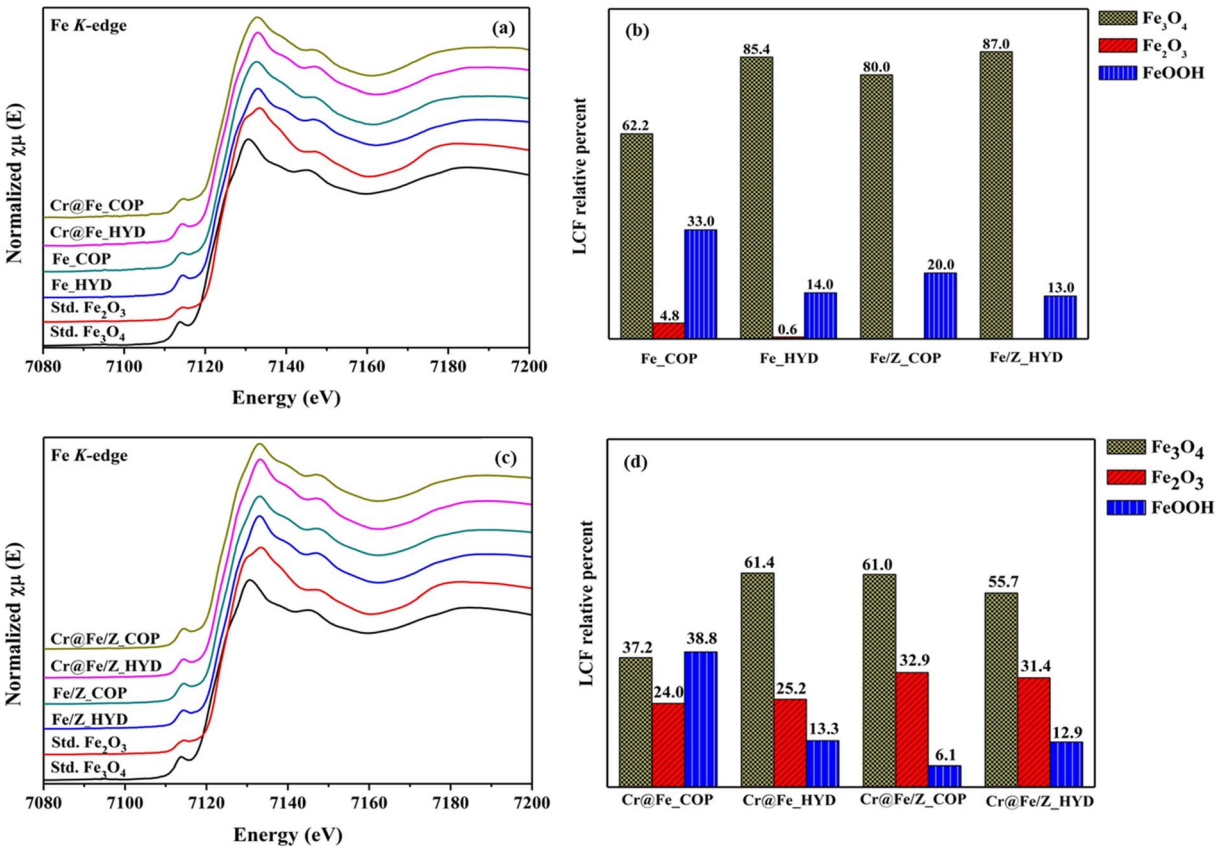

Fig. 12 Fe K-edge XANES spectra (a) and LCF (b) of Fe_HYD and Fe_COP and Fe K-edge XANES spectra (c) and LCF (d) Fe/Z_HYD and Fe/Z_COP, compared with Fe_3O_4 and Fe_2O_3 standards.

adsorption on the COP-prepared adsorbent. As a result, the Fe_3O_4 structure on Fe_HYD and Fe/Z_HYD was found to be slightly more stable.

3.4.2.3 Fe K-edge EXAFS

EXAFS of the bare absorbents. EXAFS χ^2 weight fitting of Fe K-edge was determined as shown in Fig. S2† and fitting parameters are in Table 3. The first shell of all samples revealed the short-distance Fe–O bonds in the range of 1.52–1.66 Å and the long-distance Fe–O bond of 1.93–1.97 Å presented in Fe_COP, Fe_HYD and Fe/Z_COP. The short Fe–O bond length corresponds to monomeric and dimeric ferric ion structures, including $Fe(H_2O)_6^{3+}$, $Fe(OH)(H_2O)_5^{2+}$, *trans* and *cis* $Fe(OH)_2(H_2O)_4^{+}$, $[(H_2O)_4Fe(OH)_2Fe(H_2O)_4]^{+}$, and $[(H_2O)_5FeOFe(H_2O)_5]_4^{+}$.[43] On the other hand, longer Fe–O bond distances of Fe/Z_HYD were observed at 1.89 and 2.07 Å. The results indicate that there is an accumulation of oligomers, or small clusters, of iron oxides (Fe_2O_3 and Fe_3O_4).[36] Consequently, the presence of these small clusters in Fe/Z_HYD may have significantly influenced the strong adsorption of Cr(VI) species, resulting in both a high adsorption capacity and enhanced structural stability. Meanwhile, the Fe–Fe bond in the second shell of all samples was in the range of 2.70–2.99 Å which corresponded to a typical Fe–Fe bond in Fe_2O_3 and Fe_3O_4 crystals.[44] The Fe–Fe bond length of 2.70 Å in Fe_COP is attributed to the high agglomeration of iron oxide clusters.[45]

EXAFS of the Cr-absorbed samples. The Fe K-edge EXAFS analysis and fitting parameters of the Cr-adsorbed samples are presented in Tables 4 and S2.† The Fe–O bond lengths in the six-fold coordination of Cr@Fe_HYD, Cr@Fe/Z_HYD, and Cr@Fe/Z_COP were in the range of 1.91–2.11 Å. This corresponds to the octahedral FeO_6 geometry found in typical Fe_2O_3 structures, which correlated well to LCF analysis of Fe K-edge XANES. Only the Cr@Fe_COP adsorbent exhibited longer Fe–O bonds at 2.44 Å with tetrahedral geometry (FeO_4). Additionally, the four-fold Fe–Fe bond distance was slightly longer in this sample compared to the others. These results may be attributed to the formation of an electrostatic attraction of the O_4Fe^{3+}–O–$Cr^{6+}O_4$ species on the pristine Fe_COP. However, the species were not observed on Cr@Fe/Z_COP, indicating that the zeolite support strongly interacts with iron oxide species and stabilizes them through phase transformation.

3.4.2.4 Cr K-edge XANES. A simultaneous reduction of Cr(VI) in the adsorption process of all adsorbents has been proposed. The reduction of Cr was studied on the adsorbed solid using XAS. Variation of Cr valences was determined in the XANES region using Cr_2O_3 and CrO_3 as standards for Cr^{3+} and Cr^{6+}, respectively. On adsorbent surfaces, the reduction of Cr^{6+} to Cr^{3+} on the adsorbents was identified by reduction of the pre-edge intensities in Cr K-edge XANES spectra (Fig. 14a). XANES spectra of the CrO_3 standard revealed sharp pre-edge character

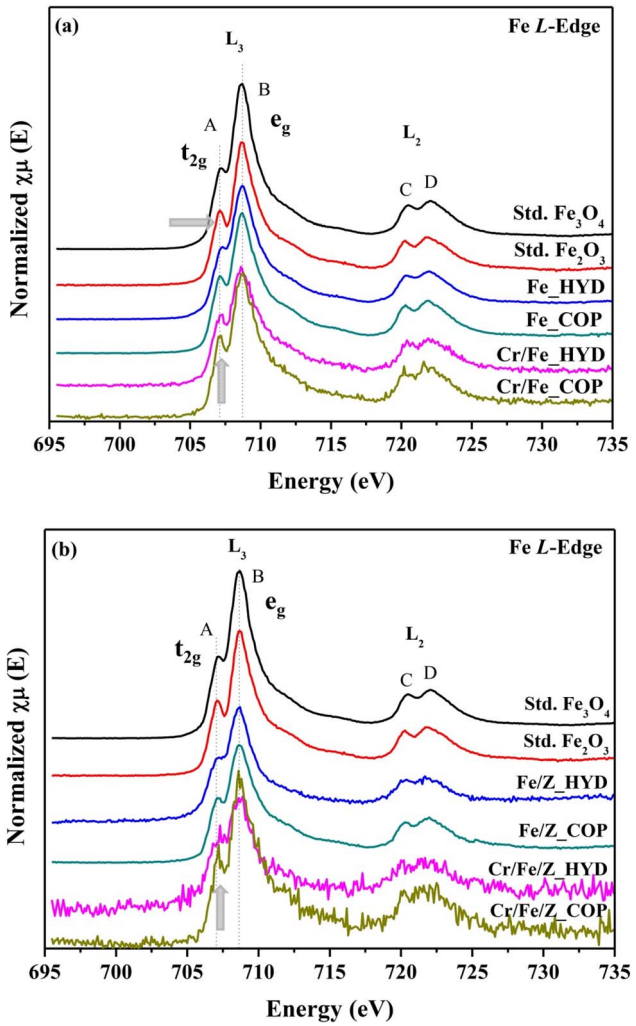

Fig. 13 Fe $L_{2,3}$-edge XANES spectra of (a) Fe_HYD and Fe_COP and (b) Fe/Z_HYD and Fe/Z_COP.

Table 3 EXAFS χ^2 weight of Fe K-edge on the bare adsorbents

Sample	Bond	R (Å)	CN	σ^2
Fe_COP	Fe–O	1.60	1.10	0.018
	Fe–O	1.97	3.10	0.002
	Fe–Fe	2.70	3.30	0.001
	Fe–O	3.37	2.40	0.014
Fe_HYD	Fe–O	1.55	1.00	0.029
	Fe–O	1.93	2.90	0.013
	Fe–Fe	2.99	1.00	0.007
	Fe–O	3.36	4.30	0.006
Fe/Z_COP	Fe–O	1.52	1.10	0.026
	Fe–O	1.95	3.10	0.017
	Fe–Fe	2.99	0.80	0.008
	Fe–O	3.39	2.20	0.002
Fe/Z_HYD	Fe–O	1.89	2.90	0.006
	Fe–O	2.07	1.20	0.012
	Fe–Fe	2.95	1.10	0.017
	Fe–O	3.44	5.90	0.009

Table 4 EXAFS χ^2 weight of Fe K-edge on the Cr-adsorbed samples

Sample	Bond	R (Å)	CN	σ^2
Cr@Fe_HYD	Fe–O	1.91	3.0	0.004
	Fe–O	2.09	3.0	0.011
	Fe–Fe	3.01	3.0	0.007
	Fe–O	3.27	6.0	0.015
Cr@Fe_COP	Fe–O	1.95	4.4	0.005
	Fe–O	2.44	4.0	0.010
	Fe–Fe	3.11	3.0	0.003
	Fe–Fe	3.36	4.0	0.001
Cr@Fe/Z_HYD	Fe–O	1.95	3.0	0.007
	Fe–O	2.11	3.0	0.029
	Fe–Fe	3.01	3.0	0.011
	Fe–Fe	3.47	3.0	0.008
Cr@Fe/Z_COP	Fe–O	1.96	3.0	0.008
	Fe–O	2.10	3.0	0.037
	Fe–Fe	3.00	3.0	0.011
	Fe–Fe	3.49	3.0	0.007

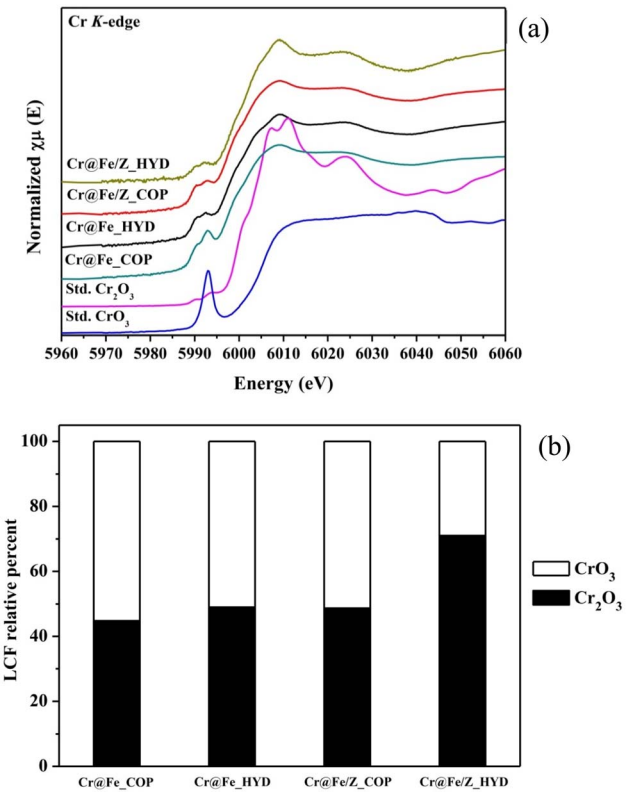

Fig. 14 Cr K-edge XANES spectra (a) and LCF (b) of Cr(VI) adsorbed samples compared with CrO_3 and Cr_2O_3 standards.

of the tetrahedral geometry Cr^{6+} at 5992.4 eV, while two pre-edge peaks with low intensity at 5989.3 and 5992.6 eV of octahedral Cr^{3+} were identified. Please take note of the following information:

All samples displayed two pre-edge positions related to Cr^{3+} with slightly higher intensity than the Cr_2O_3 standard, suggesting a partial reduction of Cr^{6+} to Cr^{3+} during the adsorption process. However, the pre-edge and XANES profiles of the samples did not align well with the Cr_2O_3 structure. To examine

the components of Cr^{6+} and Cr^{3+} in the samples, LCF analysis of the XANES spectra was conducted, as illustrated in Fig. 14b.

The samples Cr@Fe_COP, Cr@Fe_HYD, and Cr@Fe/Z_COP contained approximately 50% Cr_2O_3. Among these, the Cr@Fe/Z_HYD demonstrated the highest reduction performance of about 70%. This enhanced activity could be attributed to the well-dispersed Fe_3O_4 adsorbed species on the zeolite surface. Consequently, Cr@Fe/Z_HYD exhibited superior reduction performance and adsorption ability during the Cr^{6+} adsorption process. When supported by zeolite, the Cr^{3+} content in Cr@Fe/Z_HYD was approximately 20% higher than in Cr@Fe_HYD. The study investigated the improved Cr-reduction achieved using zeolite-supported Fe_3O_4, which was synthesized through the hydrothermal method. It was proposed that the zeolite contributes to the dispersion and stabilization of the Fe_3O_4 species.

3.4.2.5 Cr K-edge EXAFS. The Cr–O bond distances ranging from 1.66 to 1.81 Å corresponded to the Cr^{6+}–O, while the longer bond lengths at about 1.96–1.99 Å represented the Cr^{3+}–O bonds. These observations were consistent across all samples, as detailed in Table 5. Additionally, the Cr–Cr bonds at 2.98–3.03 Å were found to be longer than those in Cr_2O_3. The bond lengths were well-suited to the oligomer and small cluster of CrO_x.[46] Based on the bond distances and coordination numbers, it was suggested that an oligomeric form of $(Cr^{6+}–O–Cr^{3+}–O–Cr^{6+})_x$ could be formed on the adsorbent surface, as indicated in a report by Zine *et al.* using EPR analysis.[47] This suggested polymerization of Cr–O bonds may have been initiated by the formation of Cr^{3+} species on the surface. Notably, longer Cr–O and Cr–Cr bond distances, along with a slightly higher coordination number compared to other samples, were observed in the Cr@Fe/Z_HYD. These results suggest the formation of bonds within the CrO_x clusters. This finding aligns well with the linear combination fitting (LCF) analysis of the Cr K-edge for the sample. The presence of CrO_x clusters may enhance the adsorption stability on Cr@Fe/Z_HYD.

Structural discussion. Based on the comprehensive analysis of Fe and Cr K-edge XAS, we discuss the potential structural changes of the adsorbents during Cr adsorption. Fe_COP, Fe_HYD, Fe/Z_COP, and Fe/Z_COP contain a primary phase of Fe_3O_4 and iron oxide clusters of Fe_2O_3 and FeOOH. However, Fe/Z_HYD has larger Fe_3O_4 particle sizes with a slightly higher content determined by the Fe L_3 edge XANES, compared to the other samples. These species play a critical role in Cr-capacity and stabilization during the adsorption process. Mononuclear and binuclear species of ferric ions were found to be present in Fe_COP, Fe_HYD, and Fe/Z_COP during the adsorption process, providing an electrostatically adsorbed species of $O_4Fe^{3+}–O–Cr^{6+}O_4$. The presence of mono- and binuclear ferric species suggests an unstable iron oxide structure of the adsorbents. A partial reduction of Cr^{6+} to Cr^{3+} in the form of Fe_{1-x}-Cr_xOOH is determined in all samples. A significant cluster of CrO_x was exclusively identified in the Fe/Z_HYD adsorbent, which indicates the formation of an ion-exchange lattice composed of $Fe_{3-x}Cr_xO_4$. This structure features tetrahedral CrO_4 and octahedral CrO_6 geometries, consistent with an average coordination number of 5 for the Cr–O bonds investigated in Cr K-edge EXAFS. The presence of ion-exchange lattice species such as $Fe_{3-x}Cr_xO_4$ and $Fe_{1-x}Cr_xOOH$ aligns with the observed increase in Cr^{3+} content on Cr@Fe/Z_HYD, as demonstrated by LCF Cr K-edge XANES analysis. Consequently, the Fe/Z_HYD adsorbent enhances adsorption capacity by fostering strong interactions between Cr and the Fe_3O_4 lattice, leading to the formation of stable clusters, $Fe_{3-x}Cr_xO_4$ and $Fe_{1-x}Cr_xOOH$. This suggests that the zeolite-supported Fe_3O_4 structure prepared by the hydrothermal method improves both the Cr-adsorption capacity and stability.

Table 5 EXAFS χ^2 weight of Cr K-edge on the Cr-adsorbed samples

Sample	Bond	R (Å)	CN	σ^2
Cr@Fe_COP	Cr–O	1.75	2.0	0.032
	Cr–O	1.97	2.1	0.005
	Cr–Cr	3.00	3.0	0.020
	Cr–O	3.11	3.0	0.013
Cr@Fe_HYD	Cr–O	1.66	2.0	0.055
	Cr–O	1.99	2.1	0.005
	Cr–Cr	3.03	3.0	0.012
	Cr–O	3.16	3.0	0.005
Cr@Fe/Z_COP	Cr–O	1.78	2.0	0.041
	Cr–O	1.97	2.0	0.004
	Cr–Cr	2.98	2.8	0.016
	Cr–O	3.09	2.3	0.002
Cr@Fe/Z_HYD	Cr–O	1.81	2.4	0.018
	Cr–O	1.96	2.6	0.001
	Cr–Cr	3.03	3.3	0.014
	Cr–O	3.81	3.7	0.011

3.5. Structural stability of Fe/ZSM-5_HYD after Cr-adsorption

After chromium adsorption, the crystallinity of Fe/ZSM-5 decreased, as evidenced by the lower intensity of the main peaks, as shown in Fig. S3(A).† A significant decrease in the crystallinity of both the ZSM-5 and Fe_3O_4 phases was observed in the sample with a Si/Fe ratio of 1.1. These results indicate that Fe/ZSM-5 with high iron loading is less stable during chromium adsorption.

The FTIR spectra in Fig. S3(B)† of the Cr-adsorbed Fe/ZSM-5_HYD displayed low signal intensity due to the presence of Cr species covering the surfaces of ZSM-5, a phenomenon commonly observed in the literature regarding Cr adsorption.[48] A shoulder peak at 1223 cm^{-1} and a strong adsorption band at 1100 cm^{-1} correspond to the antisymmetric stretching vibrations of the Si–O–Si bond in ZSM-5.[49] These features were present in all samples, although a decrease in band intensities was noted, correlating well with the amounts of Cr uptake. The lowest band intensity was observed in the Fe/Z_HYD sample, which had a Si/Fe ratio of 1.1. These results were in strong agreement with the XRD intensity findings. The crystallinity of ZSM-5 significantly decreased during the chromium adsorption process in samples with high iron content. Therefore, optimal iron incorporation into the ZSM-5 structure is crucial for maintaining crystallinity during the adsorption process.

4. Conclusion

Magnetite (Fe_3O_4) and magnetite-supported ZSM-5 zeolite (Fe/Z) were successfully synthesized *via* co-precipitation and hydrothermal methods. Fe_3O_4 was observed as a major phase in all samples. The Fe_3O_4 particles prepared by different methods showed different shapes and sizes. The uniform spherical shape with large particle sizes of 400–500 nm was observed in Fe_HYD and Fe/Z_HYD. Meanwhile, rod-like and granule particle shapes with small sizes of 20–50 nm were exhibited on Fe_COP and Fe/Z_COP. The supporting zeolite could maximize the Cr-adsorption capacity of Fe_3O_4 in both preparation methods. Fe/Z_HYD adsorbent showed the most adsorption capacity of 2.33 mg per g Fe and the highest content of the reduced Cr^{3+} species over other adsorbent at 30 min and pH 2. A superior capacity of the Fe/Z_HYD was attributed to the homogenous dispersion of the Fe_3O_4 particles on zeolite and the presence of the stable Cr-adsorbed species. The stable forms of $Fe_{3-x}Cr_xO_4$ and $Fe_{1-x}Cr_xOOH$, which are an ion-change Cr into Fe_3O_4 lattice, were investigated. Fe_COP, Fe/Z_COP, and Fe_HYD exhibited unstable electrostatic attraction of Cr through mono- and binuclear ferric oxides, resulting in low adsorption capacity due to weak interaction of Cr on the adsorbent surface.

Conflicts of interest

There are no conflicts to declare.

Acknowledgements

This work was supported by the Fundamental Fund of Khon Kaen University, the National Science Research and Innovation Fund (NSRF), Center for Innovation in Chemistry (PERCH-CIC), Materials Chemistry Research Center (MCRC), Khon Kaen University, Thailand. Synchrotron Light Research Institute (SLRI), Nakhon Ratchasima, Thailand (BL 1.1W and 5.3).

References

1 A. Gaffer, A. A. Al Kahlawy and D. Aman, *Egypt. J. Pet.*, 2017, **26**, 995–999.
2 S. S. Pillai, M. D. Mullassery, N. B. Fernandez, N. Girija, P. Geetha and M. Koshy, *Ecotoxicol. Environ. Saf.*, 2013, **92**, 199–205.
3 L. N. Døssing, K. Dideriksen, S. L. S. Stipp and R. Frei, *Chem. Geol.*, 2011, **285**, 157–166.
4 M. Sun, G. Zhang, Y. Qin, M. Cao, Y. Liu, J. Li, J. Qu and H. Liu, *Environ. Sci. Technol.*, 2015, **49**, 9289–9297.
5 H.-K. Zhang, H. Lu, J. Wang, J.-T. Zhou and M. Sui, *Environ. Sci. Technol.*, 2014, **48**, 12876–12885.
6 E. Saksornchai, J. Kavinchan, S. Thongtem and T. Thongtem, *Mater. Lett.*, 2018, **213**, 138–142.
7 R. Ianoş, C. Păcurariu, S. G. Muntean, E. Muntean, M. A. Nistor and D. Nižňanský, *J. Alloys Compd.*, 2018, **741**, 1235–1246.
8 S. Rajput, C. U. Pittman and D. Mohan, *J. Colloid Interface Sci.*, 2016, **468**, 334–346.
9 K. S. Padmavathy, G. Madhu and P. V. Haseena, *Proc. Technol.*, 2016, **24**, 585–594.
10 M. R. Lasheen, I. Y. El-Sherif, D. Y. Sabry, S. T. El-Wakeel and M. F. El-Shahat, *Desalin. Water Treat.*, 2014, **52**, 6464–6473.
11 Y. C. Sharma and V. Srivastava, *J. Chem. Eng. Data*, 2011, **56**, 819–825.
12 M. Kumari, C. U. Pittman and D. Mohan, *J. Colloid Interface Sci.*, 2015, **442**, 120–132.
13 N. Senamart, K. Deekamwong, J. Wittayakun, S. Prayoonpokarach, N. Chanlek, Y. Poo-arporn, S. Wannapaiboon, P. Kidkhunthod and S. Loiha, *RSC Adv.*, 2022, **12**, 25578–25586.
14 N. T. N. Mai, N. T. A. Thu, N. T. B. Trang, P. Q. Phu, D. V. H. Thien, L. H. V. Thanh and C. L. N. Hanh, *IOP Conf. Ser.: Earth Environ. Sci.*, 2021, **947**, 012012.
15 F. Pirvu, C. I. C. Mierlă and G. A. Catrina, *J. Nanomater.*, 2023, **13**(11), 1745.
16 Q. Fang, J. W. Lin, Y. H. Zhan, M. J. Yang and W. J. Zheng, *Huan Jing Ke Xue*, 2014, **35**(8), 2992–3001.
17 N. Kordala and M. Wyszkowski, *Molecules*, 2024, **29**, 1069.
18 H. Prats, G. Alonso, R. Sayós and P. Gamallo, *Microporous Mesoporous Mater.*, 2020, 1104.
19 T. Wang, L. Liu, H. Wu, J. Zhang, Z. Feng, X. Yan, X. Wang, G. Han and X. Feng, *Dalton Trans.*, 2024, **53**, 5212.
20 J. Zhang, X. Tang, H. Yi, Q. Yu, Y. Zhang, J. Wei and Y. Yuan, *Appl. Catal., A*, 2022, **630**, 118467.
21 J. Cao, G. Chang, H. Guo and J. Chen, *Trans. Tianjin Univ.*, 2013, **19**, 326–331.
22 S. I. U. Madrid, U. Pal and F. S.-D. Jesus, *Adv. Nan. Res.*, 2014, **2**, 187–198.
23 S. H. Gurlhosur, B. Sreekanth, N. Shashidhar, R. Desai, A. Bhusanur, C. Puranik and P. S. SaiTejaswini, *Int. J. Curr. Res.*, 2018, **10**(2), 65995–65999.
24 A. C. Zimmermann, A. Mecabô, T. Fagundes and C. A. Rodrigues, *J. Hazard. Mater.*, 2010, **179**, 192–196.
25 L. Li, Y. Li, L. Cao and C. Yang, *Carbohydr. Polym.*, 2015, **125**, 206–213.
26 G. Du, Z. Li, L. Liao, R. Hanson, S. Leick, N. Hoeppner and W.-T. Jiang, *J. Hazard. Mater.*, 2012, **221–222**, 118–123.
27 M. Kiyama, *Bull. Chem. Soc. Jpn.*, 1974, **47**, 1646–1650.
28 C. Li, J. Ma, Z. Xiao, S. B. Hector, R. Liu, S. Zuo, X. Xie, A. Zhang, H. Wu and Q. Liu, *Fuel*, 2018, **218**, 59–66.
29 Database of Zeolite Structures, accessed September 21, 2024, **https://www.iza-structure.org/databases/**.
30 B. Ma, A. F. Martinez, A. Mancini and B. Lothenbach, *Cem. Concr. Res.*, 2021, **140**, 106304.
31 Y. Yang, M. Huang, J. Qian, D. Gao and X. Liang, *Sci. Rep.*, 2020, **10**, 8331.
32 J. Zhang, S. Lin, M. Han, Q. Su, L. Xia and Z. Hui, *Water*, 2020, **12**, 446.
33 G. Zolfaghari, A. Esmaili-Sari, M. Anbia, H. Younesi, S. Amirmahmoodi and A. Ghafari-Nazari, *J. Hazard. Mater.*, 2011, **192**, 1046–1055.
34 E. Darezereshki, A. k. Darban, M. Abdollahy and A. Jamshidi-Zanjani, *Environ. Nanotechnol. Monit. Manag.*, 2018, **10**, 51–62.
35 M. N. Sahmoune, *Environ. Chem. Lett.*, 2019, **17**, 697–704.

36 Z. Harrache, M. Abbas, T. Aksil and M. Trari, *Microchem. J.*, 2019, **144**, 180–189.
37 J. He, S. Hong, L. Zhang, F. Gan and Y.-S. Ho, *Fresenius Environ. Bull.*, 2010, **19**, 2651–2656.
38 S. Nasanjargal, B. A. Munkhpurev, N. Kano, H. J. Kim and Y. Ganchimeg, *J. Environ. Prot.*, 2021, **12**, 654–675.
39 J. Baltrusaitis, D. M. Cwiertny and V. H. Grassian, *Phys. Chem. Chem. Phys.*, 2007, **9**, 5542–5554.
40 A. P. Grosvenor, B. A. Kobe and N. S. McIntyre, *Surf. Sci.*, 2004, **572**, 217–227.
41 S. Wu, J. Lu, Z. Ding, N. Li, F. Fu and B. Tang, *RSC Adv.*, 2016, **6**, 82118–82130.
42 J. Li, A. Balaji and T. K. Sham, *J. Electron Spectrosc. Relat. Phenom.*, 2017, **220**, 109–113.
43 M. Zhu, B. W. Puls, C. Frandsen, J. D. Kubicki, H. Zhang and G. A. Waychunas, *Inorg. Chem.*, 2013, **52**, 6788–6797.
44 Z. Y. Wu, S. Gota, F. Jollet, M. Pollak, M. Gautier-Soyer and C. R. Natoli, *Phys. Rev. B:Condens. Matter Mater. Phys.*, 1997, **55**, 2570–2577.
45 H. Okudera, A. Yoshiasa, K. Murai, M. Okube, T. Takeda and S. Kikkawa, *J. Mineral. Petrol. Sci.*, 2012, **107**, 127–132.
46 P. G. Harrison, N. C. Lloyd, W. Daniell, C. Bailey and W. Azelee, *Chem. Mater.*, 1999, **11**, 896–909.
47 S. Khaddar-Zine, A. Ghorbel and C. Naccache, *J. Mol. Catal. Chem.*, 1999, **150**, 223–231.
48 A. S. Gning, C. Gaye, A. B. Kama, P. A. Diaw, D. D. Thiare and M. Fall, *J. Mater. Eng.*, 2024, **12**, 84–103.
49 S. M. Ebrahimi, J. S. Ghomi and M. A. Mutashar, *Main Group Met. Chem.*, 2022, **45**, 57–73.